

Accepted Manuscript

Flow Regime Characterisation of an Impinging Axisymmetric Synthetic Jet

Alan McGuinn, Rayhaan Farrelly, Tim Persoons, Darina B. Murray

PII: S0894-1777(13)00040-X

DOI: <http://dx.doi.org/10.1016/j.expthermflusci.2013.02.003>

Reference: ETF 7925

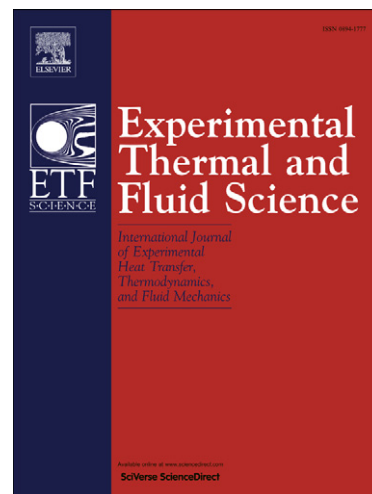
To appear in: *Experimental Thermal and Fluid Science*

Received Date: 28 January 2013

Accepted Date: 5 February 2013

Please cite this article as: A. McGuinn, R. Farrelly, T. Persoons, D.B. Murray, Flow Regime Characterisation of an Impinging Axisymmetric Synthetic Jet, *Experimental Thermal and Fluid Science* (2013), doi: <http://dx.doi.org/10.1016/j.expthermflusci.2013.02.003>

This is a PDF file of an unedited manuscript that has been accepted for publication. As a service to our customers we are providing this early version of the manuscript. The manuscript will undergo copyediting, typesetting, and review of the resulting proof before it is published in its final form. Please note that during the production process errors may be discovered which could affect the content, and all legal disclaimers that apply to the journal pertain.



Flow Regime Characterisation of an Impinging Axisymmetric Synthetic Jet

Alan McGuinn^a, Rayhaan Farrelly^a, Tim Persoons^{a,*}, Darina B. Murray^a

^a Department of Mechanical and Manufacturing Engineering, University of Dublin, Trinity College, Dublin 2, Ireland

Abstract – Impinging synthetic jets have excellent potential for energy-efficient local cooling in confined geometries. For a given geometry, synthetic jet flows are mainly characterised by the Reynolds number and the ratio of stroke length to a geometric length scale. The flow field of an impinging synthetic jet and the corresponding surface heat transfer distribution are strongly dependent on the dimensionless stroke length, yet few studies have investigated the flow field dependence for a wide range of stroke lengths. Therefore, the aim of this paper is to identify the various flow regimes as a function of stroke length. The experimental approach combines high speed particle image velocimetry and single point hot wire anemometry, and investigates an axisymmetric synthetic air jet impinging onto a smooth planar surface for a wide range of stroke length ($3 < L_0/D < 32$) and nozzle-to-surface spacing ($2 < H/D < 16$). Since the Reynolds number effect is better understood, most of the presented results are for a single Reynolds number ($Re = 1500$). Four *free synthetic jet flow morphology* regimes are identified based on threshold values for the stroke length L_0/D , which are in good agreement with previously published findings for an impulsively started jet flow. Furthermore, four *impinging synthetic jet flow regimes* are identified based on threshold values for the ratio of normalised stroke length to nozzle-to-surface spacing $(L_0 - 2D)/H$, which are in good agreement with previously published thresholds for stagnation point heat transfer regimes.

Keywords – *Particle image velocimetry; flow regimes; flow morphology; vortex; turbulence; impinging jets; synthetic jet; convective heat transfer*

* Corresponding author.

E-mail: tim.persoons@tcd.ie, Phone: +353 1 896 1936, Fax: +353 1 679 5554.

Nomenclature

1		
2		
3		
4		
5	A	cross-sectional area of orifice, m^2
6		
7	a	speed of sound, m/s
8		
9	c	velocity ratio (U_{avg}/U_{cl})
10		
11	D	orifice diameter, m
12		
13	f	frequency, Hz
14		
15		
16	f_0	Helmholtz resonance frequency, Hz
17		
18	H	nozzle-to-surface spacing, m
19		
20		
21	K	nozzle pressure loss coefficient
22		
23	L, L'	geometric and effective nozzle length, m
24		
25	L_0	synthetic jet stroke length, m
26		
27	Nu	local Nusselt number
28		
29	p_a	acoustic pressure in the synthetic jet cavity, Pa
30		
31	Re	synthetic jet Reynolds number ($= U_0 D/\nu$)
32		
33		
34	R_c	radius of curvature, m
35		
36	Sr	Strouhal number (fD/U_0)
37		
38		
39	s	swirl and shear strength parameter, s^{-2}
40		
41	t	time, s
42		
43	U, V	axial and radial velocity components, m/s
44		
45	U_0	characteristic jet velocity ($= fL_0$), m/s
46		
47	V_c	synthetic jet cavity volume, m^3
48		
49		
50	W	orifice plate radius, m
51		
52	x, r	axial and radial coordinates, m
53		
54		
55		
56		
57		
58	ε	normalised radius of curvature ($= 2R_c/D$)
59		
60		
61		
62		
63		
64		
65		

Greek symbols

ε normalised radius of curvature ($= 2R_c/D$)

1	φ	phase angle
2		
3	λ	thermal conductivity of fluid, W/(m K)
4		
5	μ	dynamic viscosity, Pa.s
6		
7	ν	kinematic viscosity, m ² /s
8		
9		
10	ρ	density, kg/m ³
11		
12	ω	vorticity, s ⁻¹
13		

Subscripts

14		
15		
16		
17	o	stagnation point or characteristic scale for synthetic jet
18		
19	avg	spatial average in orifice cross-section
20		
21	cl	orifice centreline
22		
23		
24	imp	conditions in impingement zone
25		

Superscripts

26		
27		
28		
29	(j)	synthetic jet formation
30		

Abbreviations

31		
32		
33		
34	PIV	Particle Image Velocimetry
35		
36		
37		
38		
39		

1. Introduction

1.1. Impinging synthetic jets for heat transfer applications

A phenomenon first described as an acoustical streaming around orifices was reported by Ingard and Labate [1] in 1950; this phenomenon has since gone on to be known commonly as the synthetic jet. Still considered to be a relatively new technology the synthetic jet is considered to have great potential in many practical applications and has garnered great interest from numerous modern industries including aeronautics, automotive, manufacturing and electronics, both for purposes of flow manipulation as well as heat transfer enhancement. While this paper reports mostly on the synthetic

1 jet flow evolution prior to impingement upon a horizontal surface, the ultimate interest is with regards
2 to achieving the type of jet impingement most conducive to heat transfer.

3
4 It has been well established that the two most critical parameters required to characterise a synthetic
5 jet flow are the Reynolds number $Re = \rho U_0 D / \mu$, and the dimensionless stroke length L_0 / D . These
6 characteristic velocity and length scales are defined as $L_0 = \int_{t=0}^{1/(2f)} U_{avg}(t) dt$ and $U_0 = f L_0$, where
7
8 $U_{avg}(t)$ represents the instantaneous spatially averaged velocity in the orifice and f is the jet frequency.
9
10 Much research has been undertaken into what is required to establish a jet flow with numerical and
11 experimental investigations undertaken by Holman et al. [2] and Utturkar et al. [3] where they both
12 established a jet formation criterion identifying a minimum dimensionless stroke length as the
13 determining parameter. Their results were in accordance with the previous findings of Smith and
14 Swift [4] who found that, for a two dimensional jet, a minimum dimensionless stroke length exists
15 below which no synthetic jet is formed.

16
17 Shuster and Smith [5] undertook a comprehensive investigation of a free synthetic jet flow field for
18 dimensionless stroke lengths between $1 \leq L_0 / D \leq 3$ and various Reynolds numbers. Much data were
19 presented detailing the evolution of the jet, however, with a maximum stroke length of $L_0 / D = 3$ this
20 investigation only documents behaviour for marginally formed jets. A number of other authors
21 including Glezer [6] and Gharib et al. [7] have presented data on the formation and evolution of
22 vortex rings at larger stroke lengths; these are concerned exclusively with individual rings rather than
23 an established flow. Other authors who have presented data on the evolution of the vortex ring include
24 Valiorgue et al. [8] and Smith and Glezer [9], however only Valiorgue et al. [8] documented its
25 behaviour upon impingement and only for an axial spacing of $H / D = 2$ and stroke length of $L_0 / D =$
26
27 8.7.

28
29 It has been shown for impinging continuous jets how turbulent mixing of the flow can enhance heat
30 surface transfer [10]. Since the nature of the synthetic jet flow is highly transient, it is reasonable to
31 infer that its turbulent characteristics may depend not only on Reynolds number, but also on stroke
32 length. It has been documented by Li and Zhong [11] and Kercher et al. [12] that the shape of the heat
33 transfer distribution corresponding to an impinging synthetic jet changes significantly with nozzle to
34 impingement surface spacing. Controlling the state of the flow upon impingement by changing the
35 stroke length could be used to enhance heat transfer for a particular application. Valiorgue et al. [8]
36 presented flow visualisation and heat transfer data which explored the influence of stroke length
37 relative to nozzle to surface spacing on flow regimes and convective heat transfer mechanisms for an
38
39
40
41
42
43
44
45
46
47
48
49
50
51
52
53
54
55
56
57
58
59
60
61
62
63
64
65

1 impinging synthetic jet but the study was limited to small jet to surface distances. Persoons et al. [13]
2 have extended these findings for a more comprehensive range of parameters however no flow
3 measurements were performed. Their study also gives an objective comparison of the stagnation heat
4 transfer coefficient behaviour of an axisymmetric impinging synthetic jet and correlations and data for
5 equivalent steady jets from a number of different sources.
6

7
8
9 Comprehensive reviews of heat transfer to impinging synthetic air jets have been conducted by
10 Persoons et al. [13], Gillespie et al. [14], Wang et al. [15], Pavlova and Amitay [16], Travnicek and
11 Tesar [17] amongst others. Campbell et al. [18] conducted a review of heat transfer to an impinging
12 synthetic jet for a wider range of parameters that included varying the number of jets in a jet array,
13 various levels of confinement and the addition of cross flow.
14

15
16
17 Gallas et al. [19] presented an extensive review of numerical investigations that have been conducted
18 in the area of lumped element modelling of piezoelectric-driven synthetic jet actuators. These findings
19 have recently been extended by Persoons [20] to include the concept of thermal efficiency as a
20 coefficient of performance for synthetic jet actuators, and how its frequency dependence affects the
21 optimal design and operation of synthetic jet coolers. These investigations reveal much about the
22 potential performance of the synthetic jet, however there is a lack of research which analyses the
23 behaviour of the impinging flow from its component levels, thus providing a clear basis for the
24 resulting heat transfer trends.
25
26
27
28
29
30
31
32
33
34

35 **1.2. Effect of stroke length on the flow field of a free synthetic jet**

36
37
38 The two main parameters that characterise a free axisymmetric synthetic jet are the Reynolds number
39 Re and stroke length L_0/D . It is therefore important to understand how changes in these variables
40 affect jet formation and subsequent evolution. While Shuster and Smith [5] have shown that Reynolds
41 number can have an effect on the coherence and stability of the vortex once formed, there is no
42 available evidence to suggest that Reynolds number plays a dominant role in the formation and
43 advection of the vortex. In contrast, it has been established that Strouhal number ($St = fD/U_0$) and
44 thus stroke length, plays a key role in jet formation and also significantly affects the flow field
45 characteristics, as shown by Zhou et al. [21], Glezer [6], Holman et al. [2], Shuster and Smith [5].
46
47 Furthermore, formation criteria for both symmetric and two dimensional jets have been proposed by
48 Utturkar et al. [3], Holman et al. [2], and validated by both Shuster and Smith [5] and Gallas et al.
49 [22]. It is noteworthy, however, that few authors, with the exception of Cater and Soria [23] and
50 Crittenden and Glezer [24], have investigated the effects of jet formation much beyond L_0/D of 10,
51
52
53
54
55
56
57
58
59
60
61
62
63
64
65

with neither of these documenting the evolution of an ejection. Some of the most relevant research pertaining to this field of study has been undertaken by Gharib et al. [7] where it was established that there exists a universal stroke length $L_0/D \cong 4$, also referred to as formation length, for complete vortex ring formation. Beyond this threshold stroke length no increase in vortex size was noted, with subsequently ejected fluid forming a trailing jet following the vortex. Results by Gharib et al. [7] were limited in that they presented data for impulsively started jets which is not directly comparable to the type of reciprocating flow produced by a synthetic jet. Nevertheless, this finding has significant implications for the formation and evolution of the synthetic jet.

1.3. Objectives

The aim of this paper is to investigate the dependence on the dimensionless stroke length of the flow field of an axisymmetric synthetic jet impinging perpendicularly onto a planar surface. Compared to previous studies of the flow dynamics (most of which were performed with free synthetic jets), this research covers a wide range of stroke length ($3 \leq L_0/D \leq 32$) and nozzle-to-surface spacing ($2 \leq H/D \leq 16$), which allows identification of the governing flow regimes. Flow regime identification will be done using time-resolved whole-field and single-point velocity measurements. This paper aims to provide further confirmation and explanation for the stagnation point heat transfer regimes as presented by Persoons et al. [13].

2. Experimental approach

2.1. Impinging synthetic jet test facility

The synthetic jet cavity is cylindrical in shape with an internal volume $V_c = 101.6\text{cm}^3$ (75mm internal diameter), and a sharp-edged orifice (diameter $D = 5\text{mm}$, $L = 10\text{mm}$ long). The orifice plate extends radially to $W = 10D$ from the jet centreline, providing a high level of flow confinement at small nozzle-to-surface distances, with W/H ranging between 5 ($H/D = 2$) to 0.625 ($H/D = 16$). Figure 1 shows a schematic diagram for illustration. A Visaton FR-8 (8 ohm) loudspeaker drives the jet, and is powered using a 40W audio amplifier which is supplied with a sinusoidal signal generated by a National Instruments data acquisition system.

The synthetic jet operational parameters are continuously monitored using a high-pressure microphone (G.R.A.S. 40BH, 0.5mV/Pa) which measures the acoustic pressure in the cavity p_a . This

reading is used in conjunction with a pressure-velocity calibration model described by Persoons and O'Donovan [25] to determine the orifice velocity amplitude $\|U_{avg}\|$:

$$\frac{\rho a \|U_{avg}\|}{\|P_a\|} = \sqrt{\frac{2V_c}{AL'}} \cdot \sqrt{\left(\frac{f}{f_0}\right)^2 + \left(\frac{f}{f_0}\right)^4 + \left(K \frac{V_c}{AL'} \frac{\|P_a\|}{\rho a^2}\right)^2}^{-1} \quad (1)$$

where ρ and a are the density of and speed of sound in the fluid, A and L' are the cross-sectional area and effective length of the orifice ($L' = L + 2\beta D$), and f_0 is the Helmholtz frequency ($f_0 = a/(2\pi L')(AL'/V_c)^{1/2} \cong 210$ Hz). K is an empirical constant representing the pressure loss in the orifice (here: $K = 1.46 \pm 0.13$ and $\beta = 0.425$). The model accurately predicts the jet velocity up to a geometry-dependent limit frequency which is about 2-3 times the Helmholtz frequency [25]. For excitation by a sinusoidal waveform, and based on the value of $\|U_{avg}\|$ from Eq. (1),

$$L_0 \left(= \int_{t=0}^{(2f)^{-1}} U_{avg} dt \right) = \frac{\|U_{avg}\|}{\pi f} \quad \text{and} \quad Re = \frac{\rho U_0 D}{\mu} = \frac{\rho D}{\mu} f L_0 = \frac{\rho D}{\mu} \frac{\|U_{avg}\|}{\pi} \quad (2)$$

This approach allows for adjustment of the synthetic jet operating point in terms of Reynolds number and stroke length according to Eq. (2), irrespective of changes in actuator performance. Based on the standard deviation in the measured cavity pressure and the error propagation method, the estimated uncertainty in L_0 and Re is below 5%, with a confidence level of 95%.

The synthetic jet assembly is attached to a vertical, manually operated traverse. The synthetic jet impinges onto a surface consisting of a heated copper plate (450×550mm², 5mm thick) approximating a uniform wall temperature boundary condition as verified in previous studies [13,26]. Heating is provided using a 1.1mm thick silicon heater mat which is adhered to the underside of the plate on one side and insulated on the other. The heater mat is powered using a variable voltage DC power supply and operated to provide an approximate surface temperature of 60°C.

2.2. Local fluid velocity and temperature measurements

The particle image velocimetry (PIV) system used to measure the flow velocity field employs a twin cavity Quantronix Darwin Duo high repetition Nd:YLF laser (527nm, 15mJ per pulse at 1000Hz) in conjunction with a Photron HighSpeedStar 6 CMOS digital camera (1024×1024 pixels, 12 bit per pixel, 8GB on-board memory) and a Sigma 105mm f/2.8 macro lens. A cylindrical lens and spherical telescope lens pair are used to form a light sheet of about 0.5-1mm thick, aligned perpendicular to the

1 orifice exit plane and impingement surface. The optical scaling is $39\mu\text{m}$ per pixel for $H/D \leq 8$. A
2 glycol-water aerosol is used as seeding, with particle diameters between 0.2 and 0.3 μm . At the
3 highest air velocities encountered in this study, the Stokes number of the seeding particles is less than
4 0.002, thus bias errors due to particle lag are negligible. The particle image diameter is adjusted to
5 about 2 pixel by defocusing. For each time-averaged flow field, 3118 full resolution frames were
6 captured at a frame rate of 1024Hz.
7
8
9

10
11 A Dantec 55P15 hot wire probe was used to acquire local velocity data in the impingement zone. This
12 probe has a platinum-plated tungsten wire sensor $5\mu\text{m}$ in diameter and 1.25mm in length with offset
13 prongs to allow for boundary layer measurements. A constant temperature anemometer bridge
14 (Dantec 90C10 Streamline™ CTA) was employed to control the wire temperature. As this probe was
15 operated in a thermal boundary layer it was necessary to calibrate it using a hot wire calibration
16 facility which allowed for both velocity and temperature calibration over a range of 0.1-15m/s and 20-
17 70°C. The calibration facility utilises a compressed air line feeding a computer controlled mass flow
18 controller. The air was heated using an in-line process heater prior to entering a flow conditioner,
19 from which the heated air exited with a uniform and steady velocity profile through a nozzle at which
20 the hot wire was calibrated. The hot-wire probe was positioned 0.3mm above the surface of the plate
21 and displaced by 0.6mm from the centre of the jet. Regression uncertainty across the calibrated
22 velocity and temperature range has been calculated at less than 1% over the calibration range,
23 however, the accuracy of the velocity measurement can be adversely affected by flow reversal in the
24 presence of high turbulence levels and flow oscillations [27]. Nevertheless, the single wire probe is
25 preferred over more complicated probe designs because of its ability to measure fluid velocity very
26 close (0.3mm) to the heat flux sensor without causing excessive flow disturbance.
27
28
29
30
31
32
33
34
35
36
37
38
39
40
41
42

43 Accurate velocity measurement using a hot-wire anemometer within a thermal boundary layer
44 requires simultaneous measurement of the local fluid temperature. This was performed using a Dantec
45 55P31 cold-wire temperature probe which operates as a resistance thermometer with platinum wire
46 sensor ($1\mu\text{m}$ in diameter and 0.4mm in length) in conjunction with a constant current anemometer
47 bridge (CCA). Once a low overheat (below 1°C) is applied to the probe the current can be adjusted to
48 provide maximum temperature sensitivity without further heating the wire. At approximately 10m/s
49 this probe is capable of measuring 1°C temperature fluctuation at up to 2-3kHz. A calibration, which
50 was linear in nature, was performed on the temperature probe for a range 20-60°C. Based on an
51 average operational temperature of 40°C regression uncertainty for the temperature probe is
52
53
54
55
56
57
58
59
60
61
62
63
64
65

calculated at 0.02% with a precision limit of 0.05°C. Data for both hot-wire and cold-wire probes were acquired at 8192Hz.

2.3. Processing and analysis

The PIV vector fields are obtained using LaVision DaVis 7.2 software. A multi-pass cross-correlation vector calculation was performed with interrogation window size decreasing from 64×64 pixels with 50% window overlap down to 32×32 pixels with 75% window overlap, with window deformation and Whittaker reconstruction. With this vector processing method and the optical setup described in the previous section, the estimated uncertainty on the velocity magnitude of a PIV field is about 1-2% in the high velocity region (i.e., jet core and stagnation zone) yet increases up to 10% or higher in the low velocity entrainment region. Although advanced methods such as high dynamic velocity range PIV [28] can further enhance the measurement precision, the level of precision in the high velocity regions is sufficient for the purpose of characterising flow regimes.

The vorticity averaged over a small area A is determined using an integral technique proposed by Vollmers [29]:

$$\iint_A \vec{\omega} \cdot \vec{n} \, dA = \iint_A (\vec{\nabla} \times \vec{U}) \cdot \vec{n} \, dA = \oint_{\partial A} \vec{U} \cdot d\vec{l} \quad (3)$$

where ∂A is the boundary of A and \vec{n} is the normal unit vector. Using a discretized version of Eq. (3), the resulting vorticity is a good approximation of $\omega = \frac{1}{2}(\partial V/\partial x - \partial U/\partial r)$, where positive and negative values indicate clockwise and anti-clockwise rotation respectively.

An alternative metric has been proposed by Adrian et al. [30] which was later adopted by LaVision [31] to visualise vortical flows and quantify the combined swirling and shearing strength of a vortex in a flow field. It is formally defined as the negative value of the discriminant of complex eigenvalues of the local velocity gradient tensor [30], or

$$s = -\frac{1}{4} \left(\left(\frac{\partial U}{\partial x} \right)^2 + \left(\frac{\partial V}{\partial r} \right)^2 \right) + \frac{1}{2} \frac{\partial U}{\partial x} \frac{\partial V}{\partial r} - \frac{\partial U}{\partial r} \frac{\partial V}{\partial x} \quad (4)$$

For the purpose of comparison of different data sets, s was normalised to a dimensionless quantity $sD/(fU_0)$. The time averaged value of this swirl and shear parameter was chosen for its ability to localise the position of a vortex within a flow while disregarding much of the weaker turbulent

vorticity. It proved an effective tool in identifying the trajectory and strength of the synthetic jet vortex ring, as discussed in Sect. 3.3.

3. Experimental results and discussion

All results discussed in this section were obtained for a single axisymmetric impinging synthetic jet at $Re = 1500$, $4 \leq H/D \leq 12$, $3 \leq L_0/D \leq 32$.

3.1. Time-resolved flow field at different stroke length values

Figure 2 shows the instantaneous velocity vector field and vorticity distribution for an orifice to impingement surface distance $H/D = 8$ and $Re = 1500$. The colour magnitude represents dimensionless vorticity $\omega D/U_0$. The location of the orifice is indicated by the gap at the top of the figure. φ indicates the phase angle in the jet cycle with 0° representing the time of zero orifice velocity prior to the ejection phase. Similarly, maximum ejection and suction occurs at $\varphi = 90^\circ$ and $\varphi = 270^\circ$ respectively.

For $L_0/D = 3$, Fig. 2a shows the formation of a vortex ring immediately in front of the orifice during the ejection stroke. However, no coherent vortex rings can be seen in the far field. At this small stroke length (thus high frequency since $L_0 \propto 1/f$), there is insufficient time and momentum imparted to the partially formed vortex ring to allow it fully escape the effects of the subsequent suction stroke associated with the reciprocating nature of a synthetic jet flow. Although weak vorticity is present, the far field is devoid of the type of vortex rings associated with classic synthetic jet flow; instead a diminished, turbulent net flow has been established. This flow comes from a small amount of high velocity fluid at the front of the partially formed vortex which is indicated by the arrow. Due to the omnidirectional effect of the suction stroke this fluid reaches a sufficient distance to escape its effect. The flow that is established is of diminished momentum and lacks the periodicity in the impingement zone expected of a synthetic jet flow. Similar results presented by Shuster and Smith [5] indicated that at this stroke length a fully formed synthetic jet was produced. The formation criterion proposed by Holman et al. [2] suggests that the higher formation threshold in this case can be attributed to a non-negligible radius of curvature at the orifice edge $\varepsilon = 2R_c/D$. With the present definition of stroke length and Strouhal number, the criterion by Holman et al. [2] becomes

$$\frac{1}{Sr} = \frac{L_0}{D} = \frac{32c^2(1+\varepsilon)^p}{\kappa\pi} \quad (5)$$

where the parameter c is the amplitude ratio of the spatially averaged to the centreline velocity in the orifice, the exponent $p < 1$ accounts for flow separation caused by the exit curvature and κ represents the ratio of vortex core radius to the distance between the vortex centres.

For $L_0/D = 4$, Fig. 2b shows that a coherent vortex is formed at the outer edge of the orifice which subsequently propagates towards the impingement surface. Three discrete vortex rings at increasing axial locations are clearly visible in this flow field. Maximum velocity occurs inside the core of the vortex ring. Once maximum vortex circulation has been achieved it would be expected that any fluid subsequently ejected would form a slug of fluid, or trailing jet, following the vortex ring, however none is evident in this case. As the vortex moves farther from the orifice the location of maximum velocity naturally moves towards the front of the vortex, inferring that the propagation velocity of the vortex is smaller than the jet velocity U_0 . At a distance of about $2D$ from the impingement surface, the vortices lose coherence and momentum. An accumulation of weak preceding vortices at the surface are unable to clear the impingement zone prior to the arrival of the next vortex ring, resulting in a low vorticity level in the stagnation zone. These results indicate that a significant amount of mixing of the flow occurs before impact and no high velocity core associated with the vortex ring is detectable upon impingement.

Figure 3 shows the evolution of the flow field as the stroke length is increased to $L_0/D = 8$. A significantly larger vortex is formed at this stroke length. While Gharib et al. [7] found that maximum vortex circulation was achieved at $L_0/D = 4.2$ for a starting jet, these results indicate that a synthetic jet achieves maximum circulation at a greater stroke length. At $L_0/D = 4$, a nominal amount of fluid which would otherwise contribute to vortex circulation is reingested into the orifice during the suction stroke. For $L_0/D = 8$ (Fig. 3), once the primary vortex has been fully formed and propagates away, the remaining ejected fluid takes the form of a *trailing jet*. Fig. 3a shows that the location of maximum fluid velocity occurs closer to the rear of the vortex (as indicated by the arrow), unlike for $L_0/D = 3-4$ (Fig. 2). This is because the velocity of the fluid in the trailing jet now exceeds the velocity of vortex propagation. At $\varphi = 210^\circ$ (Fig. 3b), the maximum velocity is now located in the centre of the vortex ring, while the vortex ring diameter has widened. The trailing jet at this point is less coherent and appears to undergo a degree of detachment from the primary vortex. At $\varphi = 310^\circ$ (Fig. 3c) the trailing jet has dissipated, which has also been observed by Gharib et al. [7]. In contrast to smaller stroke

lengths a coherent vortex ring with a significant amount of fluid still present in the core can be seen impinging on the surface unimpeded by the remnants of preceding ejections.

For $L_0/D = 16$, Fig. 4 shows that the trailing jet becomes more pronounced while the vortex ring accounts for a comparatively smaller fraction of the overall ejection. Peak ejection velocity now occurs long after the vortex ring is formed. Fig. 4a shows that the vortex achieves the same level of vorticity as for $L_0/D = 8$ (Fig. 3). This indicates that a universal stroke length for vortex formation does exist and has been reached in the range $8 \leq L_0/D \leq 16$. At $\varphi = 80^\circ$ (Fig. 4a), the vortex is symmetric and coherent, although the jet has not yet reached peak ejection velocity. At $\varphi = 120^\circ$ (Fig. 4b), the arrow indicates the peak velocity location within the trailing jet, about $1D$ behind the vortex centre. Similar to $L_0/D = 8$ (Fig. 3), the vortex ring spreads radially due to the higher velocity fluid in the trailing jet. However, at $L_0/D = 16$ (Fig. 4), the larger amount of fast moving fluid in the trailing jet cannot be rolled into the vortex ring. This destabilises the vortex, which is first manifested by the skewed vortex ring in Fig. 4b. By $\varphi = 170^\circ$ (Fig. 4c) the vortex ring has largely broken up, leaving a turbulent jet of fluid about to impinge upon the surface. The highly turbulent jet is wider than the vortex and trailing jet observed at smaller stroke lengths.

For $L_0/D = 32$, Fig. 5 shows a similar flow field to $L_0/D = 16$ (Fig. 4), with the vortex being broken up by the trailing jet during the ejection phase. While no coherent vortex reaches the impingement surface at these high stroke lengths, vortex roll-up is observed at the periphery of the impact zone once the jet has impinged on the surface (Fig. 5c), resulting in the observable vortices at $1.5 \leq r/D \leq 3$. The reported characteristics have been illustrated here for an orifice-to-surface spacing of $H/D = 8$ but a similar behaviour has been observed in a wide range of nozzle-to-surface distances ($4 \leq H/D \leq 12$). For small distances ($H/D < 4$), the impingement surface restricts the formation of the vortex and can significantly affect the flow development [8].

3.2. Influence of stroke length on the free jet flow morphology

Figure 6 shows a schematic illustration of the morphology of formation and evolution of the synthetic jet flow at different stroke lengths. The four flow morphology regimes are described in Table 1.

For $L_0/D < 4$ (Figs. 6a and 2a), a vortex with maximum circulation is formed at a dimensionless stroke length $L_0/D \cong 4$ as observed by Gharib et al. [7] for an impulsively starting jet. In these conditions, maximum ejection velocity occurs half way through vortex formation, and the end of the ejection phase coincides with the detachment of the vortex. Once formed, the vortex propagates away from the

1 orifice, gradually losing kinetic energy to turbulence and contracting in diameter. Compared to
 2 impulsively starting jets [7], synthetic jets experience a greater reduction in vortex strength at low
 3 stroke length ($L_0/D < 4$) since some of the ejected fluid is reingested by the suction stroke, thereby
 4 further reducing the size of the formed vortex and inhibiting its ability to propagate away from the
 5 orifice.
 6
 7

8
 9 For $4 \leq L_0/D < 8$ (Figs. 6b, 2b, 3), the behaviour of synthetic jets markedly differs from that of
 10 impulsively started jets, where the vortex circulation does not further increase beyond $L_0/D > 4$ [7]. In
 11 case of a synthetic jet, a trailing jet is formed after the vortex detaches from the orifice. The peak
 12 velocity occurs at the interface between the vortex and trailing jet, which leads to a widening of the
 13 vortex ring as the faster moving fluid adds to the momentum of the vortex, eventually leaving a
 14 weakened lower velocity trailing jet. The stronger vortex maintains coherence longer than those
 15 formed at smaller stroke lengths, which is shown in Fig. 3 for the upper limit $L_0/D = 8$.
 16
 17

18 For $8 \leq L_0/D < 16$ (Figs. 6c, 4), vortex formation occupies only a small fraction of the ejection phase
 19 compared with the quantity of fluid ejected in the form of the trailing jet. The peak ejection velocity
 20 occurs after the vortex has detached, leading to an accelerating trailing jet which catches up on the
 21 vortex. This collision (i) increases the vortex circulation which results in a wider vortex ring diameter,
 22 (ii) yet it also destabilises the vortex, manifested by a skewing of the vortex ring followed by vigorous
 23 mixing as shown in Fig. 4. Gharib et al. [7] documented this phenomenon in starting jets up to $L_0/D <$
 24 12. Upon impact of the trailing jet on the vortex, they observed a temporary increases in vortex
 25 circulation before excess vorticity is shed or the vortex disintegrates completely. For $L_0/D \geq 16$ (Figs.
 26 6d, 5), the above phenomenon is even more pronounced, leading to complete vortex disintegration by
 27 a highly turbulent trailing jet, as shown in Fig. 5.
 28
 29
 30
 31
 32
 33
 34
 35
 36
 37
 38
 39
 40
 41
 42
 43

44 3.3. Influence of stroke length on the impinging jet flow regimes

45 The strength and propagation trajectory of the vortex in an impinging synthetic jet flow depends on a
 46 number of aspects (e.g., jet formation characteristics, interaction with a trailing jet, vortex rollup upon
 47 impingement). The dependence of the free jet flow morphology on stroke length has been shown by
 48 the instantaneous flow field results in Figs. 2-5. Building on those findings, this section further
 49 quantifies vortex strength and trajectory to identify *impinging jet flow regimes* as a function of stroke
 50 length.
 51
 52
 53
 54
 55
 56
 57

58 Figure 7 presents distributions of the time-averaged swirl and shear strength s , defined by Eq. (4). The
 59 values are normalised as $sD/(fU_0)$ and shown as a colour distribution with contour lines at $sD/(fU_0) =$
 60
 61
 62
 63
 64
 65

1
2
3
4
5
6
7
8
9
10
11
12
13
14
15
16
17
18
19
20
21
22
23
24
25
26
27
28
29
30
31
32
33
34
35
36
37
38
39
40
41
42
43
44
45
46
47
48
49
50
51
52
53
54
55
56
57
58
59
60
61
62
63
64
65

0.01, 0.1, 1 and 5. These results are computed from the same time resolved PIV data presented previously (Figs. 2-5). The grey lines represent time-averaged velocity streamlines, showing the mean flow direction and recirculation patterns. The measurements are time-averaged over a period of 3 seconds as determined by the on-board memory capacity of the high speed camera. The time-averaged flow fields are still slightly asymmetric because the synthetic jet flow is sensitive to minor geometric imperfections (e.g., curvature radius of the orifice edges).

For the smallest stroke length $L_0/D = 3$ (Fig. 7a) corresponding to free jet flow morphology (a) (Table 1, Fig. 6a), the swirl and shear strength does not extend much beyond the surrounds of the orifice, although there is a low level mean flow in the direction of the surface. Instantaneous flow fields (Fig. 2a) revealed that this was due to partial re-ingestion of the vortex during the suction stroke. For a similar synthetic jet at $L_0/D = 3$, Shuster and Smith [5] observed that the vortex travelled a distance of $3.3D$ from the orifice. Fig. 7a shows only weak swirl strength at this axial location, suggesting that the vortex ring often fails to escape the effects of the suction phase.

For $L_0/D = 4$ (Fig. 7b) corresponding to the free jet flow morphology (b) (Table 1, Fig. 6b), the flow shows a significant increase in swirl and shear strength which reaches to about $4D$ from the nozzle, yet does not reach the impingement surface. As the vortex ring detaches from the orifice the intensity reduces and the vortex ring narrows, indicating that kinetic energy is being dissipated before a coherent vortex can impinge. Although not shown here, experimental data for smaller nozzle-to-surface spacing of $H/D = 4$ confirm that coherent vortices formed at these conditions do reach the impingement surface. For the same free jet morphology (b) yet higher stroke length $L_0/D = 6$ (Fig. 7c), a coherent vortex does reach the impingement surface at $H/D = 8$.

For $L_0/D = 8$ (Fig. 7d) corresponding to the free jet flow morphology (c) (Table 1, Fig. 6c), a more powerful vortex ring impacts upon the surface. This flow regime is still dominated by successively impinging vortices, yet a further increase in stroke length beyond $L_0/D > 8$ sees a transition to a regime dominated by the trailing jet.

For $L_0/D = 16$ (Fig. 7e) corresponding to the free jet flow morphology (d) (Table 1, Fig. 6d), the vortex path widens significantly as it approaches the impingement surface. This is due to the higher velocity fluid in the trailing jet which impacts upon the vortex. Since there is no net increase in volume flux between stroke lengths, a widening of the jet is accompanied by a reduction in average velocity upon impingement. Figures 7e and 7f show that enough kinetic energy remains after

impingement to form rollup vortices in the wall jet, as indicated by the increase in swirl and shear strength near the surface up to $r/D < 5$ (see Fig. 5c).

4. Relationship between flow and heat transfer regimes

To evaluate the jet flow upon impingement, the local fluid velocity magnitude V_{imp} was recorded using a hot wire anemometer positioned close to the stagnation point (0.3mm above the surface, and 0.6mm from the jet centreline). As described in the experimental methodology, simultaneous local fluid temperature data were recorded to correct for operation within a thermal boundary layer.

Because of the close proximity to the surface (0.3mm), this method proved more accurate than relying on PIV measurements.

Figure 8a ($H/D = 8$, $Re = 1500$) shows that the maximum fluid velocity experienced in the impingement zone is achieved for $L_0/D = 6$ (Fig. 7c). The vertical dashed line represents the vortex formation threshold in this study ($L_0 = L_0^{(f)} = 2D$). Smaller stroke lengths impart less momentum to the vortex ring, causing a low velocity diminished impingement. Higher stroke lengths result in a widening of the flow, causing a reduction in stagnation point velocity.

For a wider range of $2 \leq H/D \leq 16$, Fig. 8b shows that the stroke length at which maximum impingement velocity occurs roughly scales with the nozzle-to-surface distance. To visualise this, the data are plotted by recasting the stroke length in the form used by Persoons et al. [13] to identify heat transfer regimes, as $(L_0 - L_0^{(f)})/H$, where $L_0^{(f)}$ represents the jet formation stroke length. Persoons et al. [13] found the stagnation point heat transfer coefficient data to collapse well for $L_0^{(f)} = 1.5D$, however in the current study a value of $L_0^{(f)} = 2D$ provides a better agreement for the flow field results.

As shown in Fig. 8b, the stroke lengths for maximum impingement velocity line up well to $(L_0 - L_0^{(f)})/H \cong 0.5$, which is in excellent agreement with the threshold found by Persoons et al. [13] for the regime where heat transfer is strongly dependent on stroke length and reaches a local maximum. The capital letters A, B, C, D in Fig. 8b correspond to the four impingement flow regimes identified in this study, as summarized in Table 2.

The trends presented in Fig. 8b show a remarkable agreement with stagnation point Nusselt number (Nu_0) data presented by Persoons et al. [13], as shown in Fig. 9. To only show the effect of stroke length, the vertical axis in Fig. 9 depicts Nu_0 as a Frössling number, removing the effect of Reynolds number and nozzle-to-surface spacing. The markers represent experimental data obtained in the same

1 test facility for a similar range of synthetic jet operating conditions. For clarity, only data for three
 2 H/D values are shown, yet more details are available in Persoons et al. [13]. The solid line in Fig. 9
 3 represents a correlation which is least squares fitted to the experimental data with a coefficient of
 4 determination $R^2 > 0.8$ [13]. The letters A-D indicate four heat transfer regimes, identified based on
 5 the data collapsing to this correlation expressed as a function of the ratio of stroke length to nozzle-to-
 6 surface spacing.
 7
 8
 9
 10

11 Although the regimes in Fig. 9 are determined entirely from stagnation point heat transfer results,
 12 there is a strong similarity in the trends for heat transfer regimes A and B in Fig. 9 and the impinging
 13 jet flow regimes A and B identified in Fig. 8. The division between regimes C and D in Fig. 9 was
 14 proposed by Persoons et al. [13] without information on the flow field. However, combining the
 15 insight from whole-field flow visualisations and local stagnation zone velocity measurements, it
 16 seems appropriate to adjust the regime boundary to that defined in Table 2.
 17
 18
 19
 20
 21
 22

23 Figure 10 shows a flow regime map based on PIV data, to further elucidate the impingement flow
 24 regimes. The dashed line indicates the jet formation threshold at $L_0 = L_0^{(f)} = 2D$. The dash-dotted lines
 25 represents the thresholds between the regimes A through D (see Fig. 8b and Table 2). For instance,
 26 the lowest dash-dotted line represents $(L_0 - L_0^{(f)})/H = 0.5$. This threshold indicates whether sufficient
 27 impulse is imparted to the fluid for the vortices to reach the impingement surface relatively
 28 undiminished. The square markers (\square) below this line correspond to experimental conditions where
 29 swirl and shear strength data showed that the jet possessed insufficient momentum to impact upon the
 30 surface undiminished (e.g., Figs. 2, 7a,b). Regime A identified in this study (Fig. 8) and by Persoons
 31 et al. [13] (Fig. 9) agrees very well with these observations.
 32
 33
 34
 35
 36
 37
 38
 39
 40

41 The circular markers (\circ) in Fig. 10 are in good agreement with regime B (see Figs. 8 and 9). In this
 42 regime, a reduction in impingement velocity is accompanied by a widening of the vortex ring,
 43 spreading the impinging fluid over a greater area and effectively reducing fluid velocity near the
 44 stagnation point, as shown in Figs. 3 and 7c,d. The horizontal solid line at $L_0/D = 8$ indicates the
 45 threshold between the (free) jet flow morphology regimes (a,b) and (c,d), as identified in Table 1.
 46
 47
 48
 49
 50
 51
 52
 53

54 The triangular markers (\triangle) in Fig. 10 match the regimes C and D, corresponding to Figs. 4, 5 and
 55 7e,f. In these regimes, the trailing jet dominates the impingement either by disrupting the vortex prior
 56 to impingement (Fig. 4), or by leading with the bulk of fluid in the core while the vortex is pushed to
 57 the periphery (Fig. 5). However, there is some variability in these regimes as demonstrated by the
 58
 59
 60
 61
 62
 63
 64
 65

1
2
3
4
5
6
7
8
9
10
11
12
13
14
15
16
17
18
19
20
21
22
23
24
25
26
27
28
29
30
31
32
33
34
35
36
37
38
39
40
41
42
43
44
45
46
47
48
49
50
51
52
53
54
55
56
57
58
59
60
61
62
63
64
65

triangular marker at $L_0/D = 12$ and $H/D = 12$ which falls within the bounds of regime B yet exhibits the characteristics of regimes C and D.

5. Conclusion

Using a combination of high speed particle image velocimetry and single point hot wire anemometry, this study has identified the flow morphology of a developing synthetic jet flow for a wide range of dimensionless stroke length ($3 < L_0/D < 32$) and nozzle-to-surface spacing ($2 < H/D < 16$).

Four *free synthetic jet flow morphology* regimes are identified based on threshold values for the stroke length L_0/D (see Table 1). These limits are in good agreement with findings of Gharib et al. [7] for an impulsively started jet flow. Beyond a critical stroke length of $L_0/D = 8$, a trailing jet is formed which adversely affects the stability of the primary vortex. The influence of the trailing jet increases with stroke length, and for $L_0/D > 16$ the vortex rapidly loses coherence and becomes engulfed in a turbulent unresolved intermittent jet flow.

Furthermore, four *impinging synthetic jet flow regimes* are identified based on threshold values for the ratio of stroke length to nozzle-to-surface spacing $(L_0 - L_0^{(f)})/H$, where the jet formation threshold in this study is found to be $L_0 = L_0^{(f)} = 2D$. Threshold values of $(L_0 - L_0^{(f)})/H = 0.5, 1$ and 2 delineate the four impinging jet regimes identified here (see Table 2). The time-averaged swirl and shear strength parameter $sD/(fU_0)$, where s is defined by Eq. (4), has proven useful in identifying the impinging synthetic jet flow regimes.

These regimes are in good agreement with the stagnation point heat transfer regimes presented by Persoons et al. [13], although no flow field information was used by Persoons et al. [13] in establishing their thresholds.

The results indicate that a high degree of variability in the flow field for an impinging synthetic jet is achievable by changing the dimensionless stroke length. Consequently, for any given Reynolds number and nozzle-to-surface spacing, different impinging jet flow regimes and corresponding heat transfer regimes can be achieved and potentially optimised by adjusting the stroke length. This confers a greater degree of control for synthetic jets than is present for steady jets.

Acknowledgments

Dr. Tim Persoons is a Marie Curie Fellow of the Irish Research Council. The authors acknowledge the financial support of Science Foundation Ireland (Grant no. 07/RFP/ENM123).

References

- [1] U. Ingard, H. Ising, Acoustic Nonlinearity of an Orifice, *J. Acoust. Soc. Am.* 42 (1967) 6-17.
- [2] R. Holman, Y. Utturkar, R. Mittal, B.L. Smith, L. Cattafesta, Formation Criterion for Synthetic Jets, *AIAA J.* 43 (2005) 2110-2117.
- [3] Y. Utturkar, R. Holman, R. Mittal, B. Carroll, M. Sheplak, L. Cattafesta, et al., A Jet Formation Criterion for Synthetic Jet Actuators, in: 41st Aerospace Sciences Meeting & Exhibit, Reno, NV, 6-9 Jan., 2003: AIAA Paper 2003-0636.
- [4] B.L. Smith, G.W. Swift, Synthetic Jets at Large Reynolds Number and Comparison to Continuous Jets, in: 31st AIAA Fluid Dynamics Conference, Anaheim, CA, 2001: AIAA Paper 2001-3030.
- [5] J.M. Shuster, D.R. Smith, Experimental study of the formation and scaling of a round synthetic jet, *Phys. Fluids* 19 (2007) 045109.
- [6] A. Glezer, The Formation of Vortex Rings, *Phys. Fluids* 31 (1988) 3532-3542.
- [7] M. Gharib, E. Rambod, K. Shariff, A universal time scale for vortex ring formation, *J. Fluid Mech.* 360 (1998) 121-140.
- [8] P. Valiorgue, T. Persoons, A. McGuinn, D.B. Murray, Heat transfer mechanisms in an impinging synthetic jet for a small jet-to-surface spacing, *Exp. Therm. Fluid Sci.* 33 (2009) 597-603.
- [9] B.L. Smith, A. Glezer, The formation and evolution of synthetic jets, *Phys. Fluids* 10 (1998) 2281-2297.
- [10] T.S. O'Donovan, D.B. Murray, A.A. Torrance, Impinging jet heat transfer in the transitional wall jet region, in: ASME Summer Heat Transfer Conference, San Francisco, CA, 2005: HT2005-72451.
- [11] M. Li, S. Zhong, Heat transfer and flow characteristics of impinging synthetic jets, in: 9th UK National Heat Transfer Conference, 2005.
- [12] D.S. Kercher, J.B. Lee, O. Brand, M.G. Allen, A. Glezer, Microjet cooling devices for thermal management of electronics, *IEEE Trans. Compon. Packag. Technol.* 26 (2003) 359-366.
- [13] T. Persoons, A. McGuinn, R. Farrelly, D.B. Murray, A general correlation for the stagnation point Nusselt number of an axisymmetric impinging synthetic jet, *Int. J. Heat Mass Transfer* 54 (2011) 3900-3908.

- 1
2
3
4
5
6
7
8
9
10
11
12
13
14
15
16
17
18
19
20
21
22
23
24
25
26
27
28
29
30
31
32
33
34
35
36
37
38
39
40
41
42
43
44
45
46
47
48
49
50
51
52
53
54
55
56
57
58
59
60
61
62
63
64
65
- [14] M.B. Gillespie, W.Z. Black, C. Rinehart, A. Glezer, Local convective heat transfer from a constant heat flux flat plate cooled by synthetic air jets, *J. Heat Transfer-Trans. ASME*. 128 (2006) 990-1000.
- [15] Y. Wang, G. Yuan, Y.-K. Yoon, M.G. Allen, S.A. Bidstrup, Optimization of Synthetic Jet Fluidic Structures in Printed Wiring Boards, *J. Electron. Packag.* 128 (2006) 353-359.
- [16] A. Pavlova, M. Amitay, Electronic cooling using synthetic jet impingement, *J. Heat Transfer*, 128 (2006) 897-907.
- [17] Z. Travnicek, V. Tesar, Annular synthetic jet used for impinging flow mass transfer, *Int. J. Heat Mass Transfer* 46 (17) (2003) 3291-3297.
- [18] J.S. Campbell, W.Z. Black, A. Glezer, J.G. Hartley, Thermal Management of a Laptop Computer with Synthetic Air Microjets, in: *IEEE Intersoc. Conf. Therm. Phenom.*, 1998: pp. 43-50.
- [19] Q. Gallas, B. Carroll, L. Cattafesta, R. Holman, T. Nishida, M. Sheplak, Lumped Element Modeling of Piezoelectric-Driven Synthetic Jet Actuators, *AIAA J.* 41 (2003) 240-247.
- [20] T. Persoons, General reduced-order model to design and operate synthetic jet actuators, *AIAA J.* 50 (2012) 916-927.
- [21] J. Zhou, H. Tang, S. Zhong, Vortex Roll-Up Criterion for Synthetic Jets, *AIAA J.* 47 (2009) 1252-1262.
- [22] Q. Gallas, R. Holman, R. Raju, R. Mittal, M. Sheplak, L. Cattafesta, Low Dimensional Modeling of Zero-Net Mass-Flux Actuators, in: *2nd AIAA Flow Control Conference*, Portland, OR, 28 June-1 July, 2004: AIAA Paper 2004-2413.
- [23] J.E. Cater, J. Soria, The evolution of round zero-net-mass-flux jets, *J. Fluid Mech.* 472 (2002) 167-200.
- [24] T.M. Crittenden, A. Glezer, A high-speed, compressible synthetic jet, *Phys. Fluids* 18 (2006) 017107.
- [25] T. Persoons, T.S. O'Donovan, A pressure-based estimate of synthetic jet velocity, *Phys. Fluids*. 19 (2007) 128104.
- [26] T.S. O'Donovan, D.B. Murray, Jet impingement heat transfer - Part I: Mean and root-mean-square heat transfer and velocity distributions, *Int. J. Heat Mass Transfer* 50 (2006) 3291-3301.
- [27] T. Persoons, A. Hoefnagels, E. Van den Bulck, Calibration of an oscillating hot-wire anemometer for bidirectional velocity measurements, *Exp. Fluids* 40 (2006) 555-567.
- [28] T. Persoons, T. S. O'Donovan, High dynamic velocity range particle image velocimetry using multiple pulse separation imaging, *Sensors* 11 (2011) 1-18.
- [29] H. Vollmers, Detection of vortices and quantitative evaluation of their main parameters from experimental velocity data, *Meas. Sci. Technol.* 12 (2001) 1199-1207.
- [30] R.J. Adrian, K.T. Christensen, Z.C. Liu, Analysis and interpretation of instantaneous turbulent velocity fields, *Exp. Fluids* 29 (2000) 275-290.
- [31] Davis 7.2 Software Manual, Lavision GmbH, 2009: Göttingen, Germany.

List of Tables

Table 1. Free synthetic jet flow morphology regimes as a function of stroke length (see Fig. 6).

Regime	Stroke length threshold	Corresponding figures	Description
	$L_0 \leq L_0^{(f)} (= 2D)$		No jet formed below the formation threshold stroke length ^{**} .
(a)	$L_0^{(f)}/D < L_0/D \leq 4$	Fig. 2a,b	Monotonous increase in vortex strength with stroke length up to a maximum at $L_0/D = 4$.
(b)	$4 < L_0/D \leq 8$	Fig. 3	Additional ejected fluid (beyond $L_0/D = 4$) forms a trailing jet following the vortex, resulting in a wider vortex core.
(c)	$8 < L_0/D \leq 16$	Fig. 4	Maximum ejection velocity occurs in the trailing jet, which destabilises the preceding vortex and results in increased flow mixing.
(d)	$L_0/D > 16$	Fig. 5	The flow is dominated by the trailing jet which overtakes the vortex, resulting in a highly turbulent intermittent jet flow.

^{**} The formation threshold value $L_0^{(f)}/D = 2$ found in this study is higher than the limit proposed by e.g. Holman et al. [2], which may be attributed to minor geometric differences (e.g., a rounded orifice edge, see Eq. (4)).

Table 2. Impinging synthetic jet flow regimes as a function of stroke length (see Fig. 8).

Regime	Stroke length threshold	Corresponding figures	Description
	$L_0 \leq L_0^{(f)} (= 2D)$		No jet formed below the formation threshold stroke length ^{**} .
A	$0 < (L_0 - L_0^{(f)})/H \leq 0.5$	Fig. 7a,b	Diminishing impingement due to insufficient fluid momentum near the surface.
B	$0.5 < (L_0 - L_0^{(f)})/H \leq 1$	Fig. 7c,d	Optimal impingement for maximum stagnation point velocity.
C	$1 < (L_0 - L_0^{(f)})/H \leq 2$	Fig. 7e	Radial spreading/widening of the jet causing reduction in time-averaged velocity approaching the stagnation point.
D	$(L_0 - L_0^{(f)})/H > 2$	Fig. 7f	Regime dominated by the trailing jet.

^{**} The formation threshold value $L_0^{(f)}/D = 2$ found in this study is higher than the limit proposed by e.g. Holman et al. [2], which may be attributed to minor geometric differences (e.g., a rounded orifice edge, see Eq. (4)).

List of Figure Captions

Fig. 1. Schematic diagram of the impinging synthetic jet facility.

Fig. 2. Instantaneous flow field ($H/D = 8$, $Re = 1500$) showing the distribution of vorticity $\omega D/U_0$ and velocity vectors, with the arrow indicating the location of highest velocity magnitude. (a) $L_0/D = 3$ (at $\varphi = 140^\circ$), (b) $L_0/D = 4$ (at $\varphi = 100^\circ$)

Fig. 3. Instantaneous flow field ($H/D = 8$, $Re = 1500$) at $L_0/D = 8$ showing the distribution of vorticity $\omega D/U_0$ and velocity vectors, with the arrow indicating the location of highest velocity magnitude. (a) $\varphi = 140^\circ$, (b) $\varphi = 210^\circ$, (c) $\varphi = 310^\circ$.

Fig. 4. Instantaneous flow field ($H/D = 8$, $Re = 1500$) at $L_0/D = 16$ showing the distribution of vorticity $\omega D/U_0$ and velocity vectors, with the arrow indicating the location of highest velocity magnitude. (a) $\varphi = 80^\circ$, (b) $\varphi = 120^\circ$, (c) $\varphi = 170^\circ$.

Fig. 5. Instantaneous flow field ($H/D = 8$, $Re = 1500$) at $L_0/D = 32$ showing the distribution of vorticity $\omega D/U_0$ and velocity vectors, with the arrow indicating the location of highest velocity magnitude. (a) $\varphi = 70^\circ$, (b) $\varphi = 90^\circ$, (c) $\varphi = 130^\circ$.

Fig. 6. Flow morphology of vortex formation and evolution at various stroke lengths (a) $L_0/D < 4$, (b) $4 \leq L_0/D < 8$, (c) $8 \leq L_0/D < 16$, (d) $L_0/D \geq 16$ (see Table 1).

Fig. 7. Distributions of the time-averaged swirl and shear strength $sD/(fU_0)$ (Eq. (4)) and velocity streamlines for $H/D = 8$, $Re = 1500$. (a) $L_0/D = 3$, (b) $L_0/D = 4$, (c) $L_0/D = 6$, (d) $L_0/D = 8$, (e) $L_0/D = 16$, (f) $L_0/D = 32$.

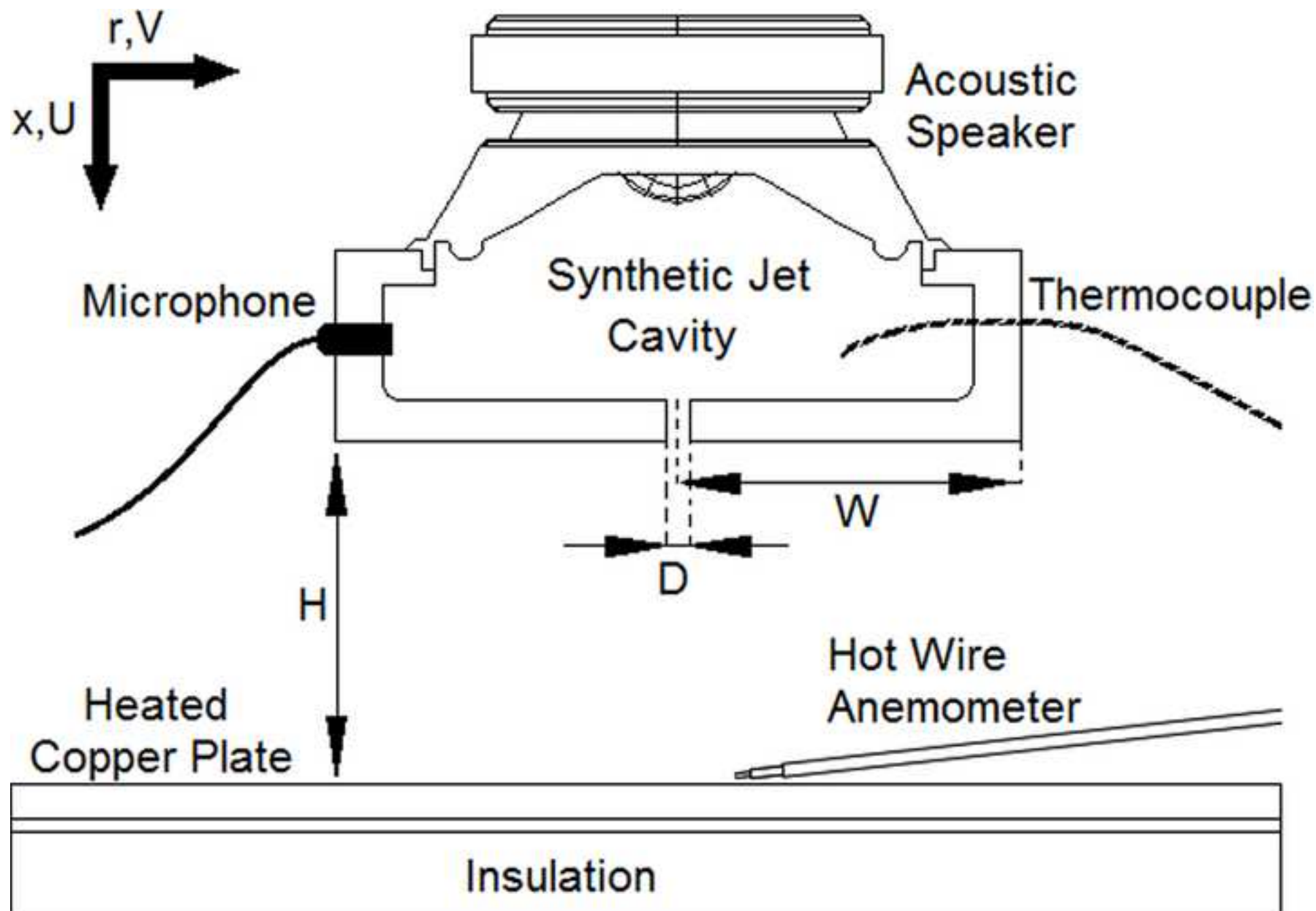
Fig. 8. Near stagnation point impingement velocity V_{imp}/U_0 measured using a hot-wire anemometer probe at 0.3mm ($0.06D$) above the impingement surface and $r/D = 0.12$; (a) $H/D = 8$, $Re = 1500$, (b) $2 \leq H/D \leq 16$, $Re = 1500$. Capital letters A, B, C, D correspond to four impinging jet flow regimes in Table 2. Markers represent $H/D = 2$ (\triangleleft), 3 (\triangleright), 4 (\star), 6 (\triangle), 8 (∇), 10 (\times), 12 (\square), 16 (\circ).

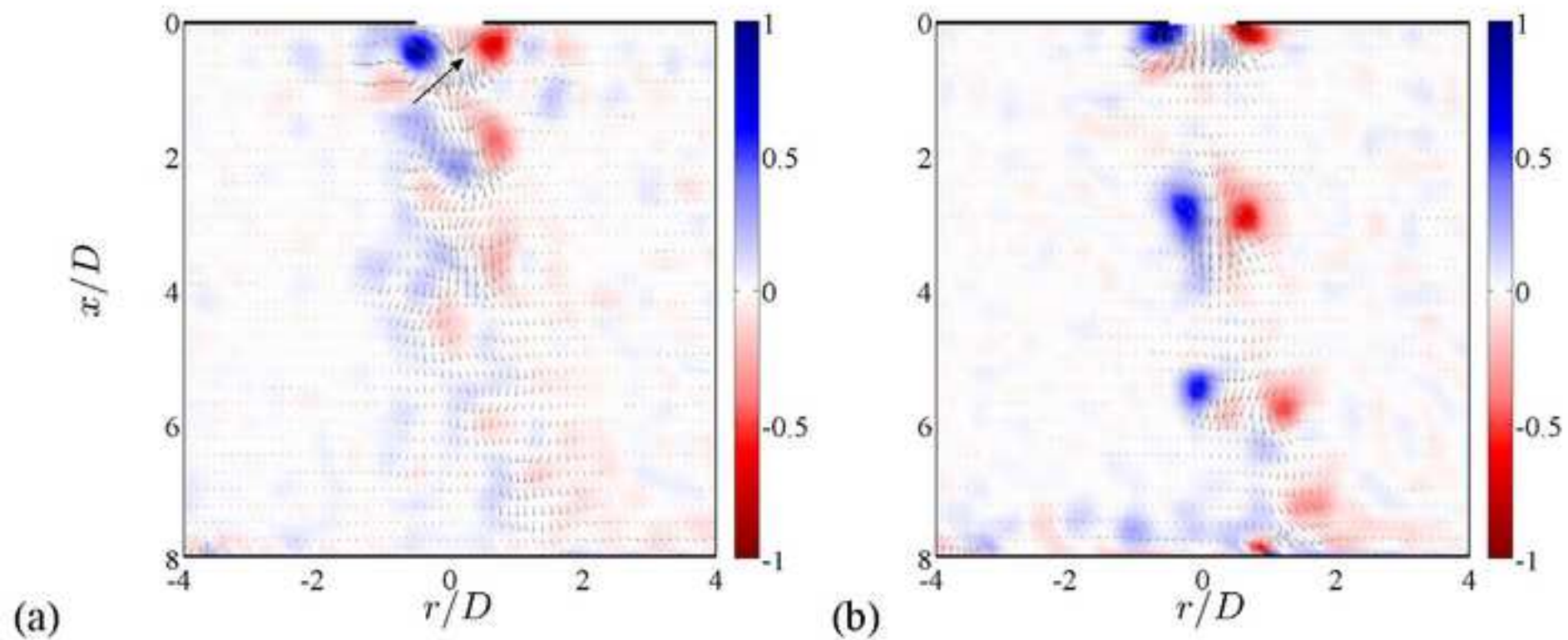
Fig. 9. Dependence of stagnation point Nusselt number $Nu_0/(Re^m Pr^n f(H))$ on stroke length ($L_0 - L_0^{(f)}/H$ (where $L_0^{(f)} = 1.5D$ [13]) for $4 \leq H/D \leq 12$, $Re = 1500$. Capital letters A, B, C, D represent four

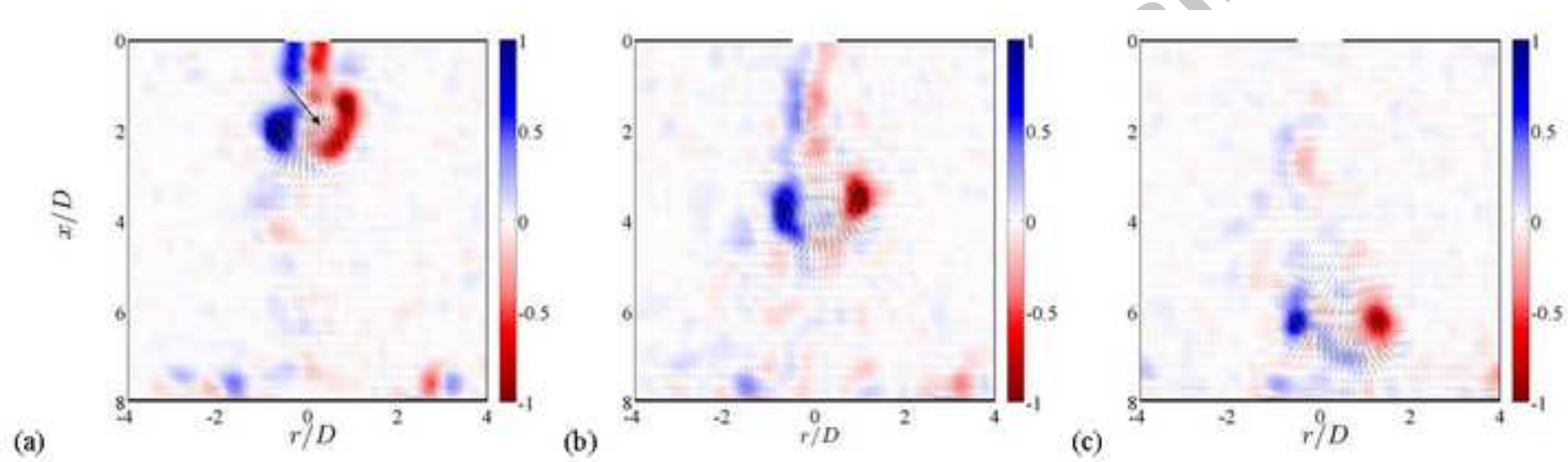
1
2
3
4
5
6
7
8
9
10
11
12
13
14
15
16
17
18
19
20
21
22
23
24
25
26
27
28
29
30
31
32
33
34
35
36
37
38
39
40
41
42
43
44
45
46
47
48
49
50
51
52
53
54
55
56
57
58
59
60
61
62
63
64
65

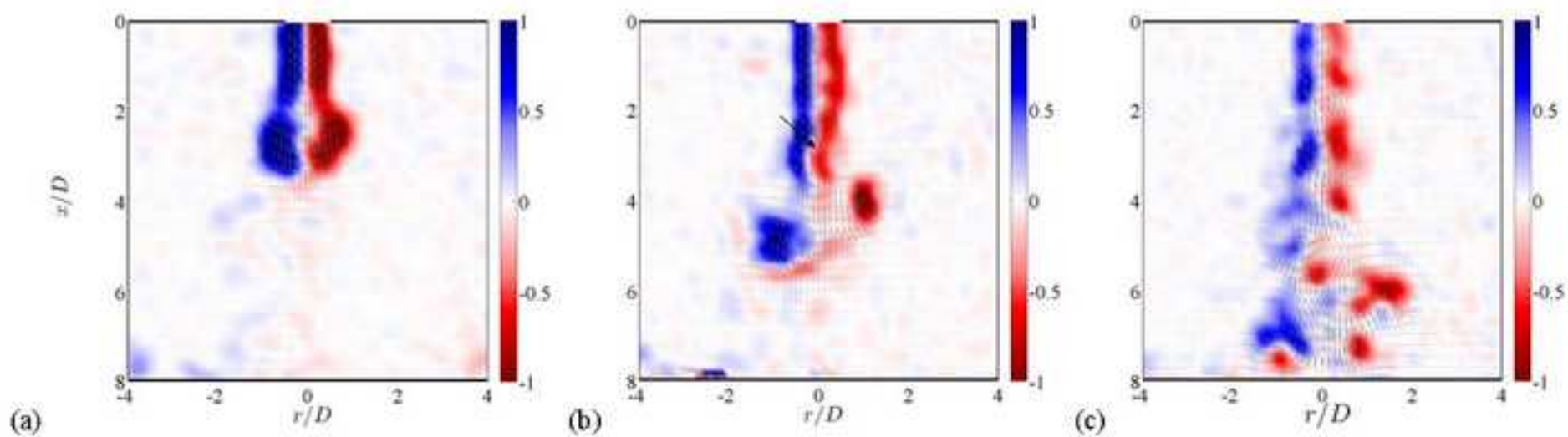
heat transfer regimes identified by Persoons et al. [13], which are in close agreement with the corresponding regimes in Table 2.

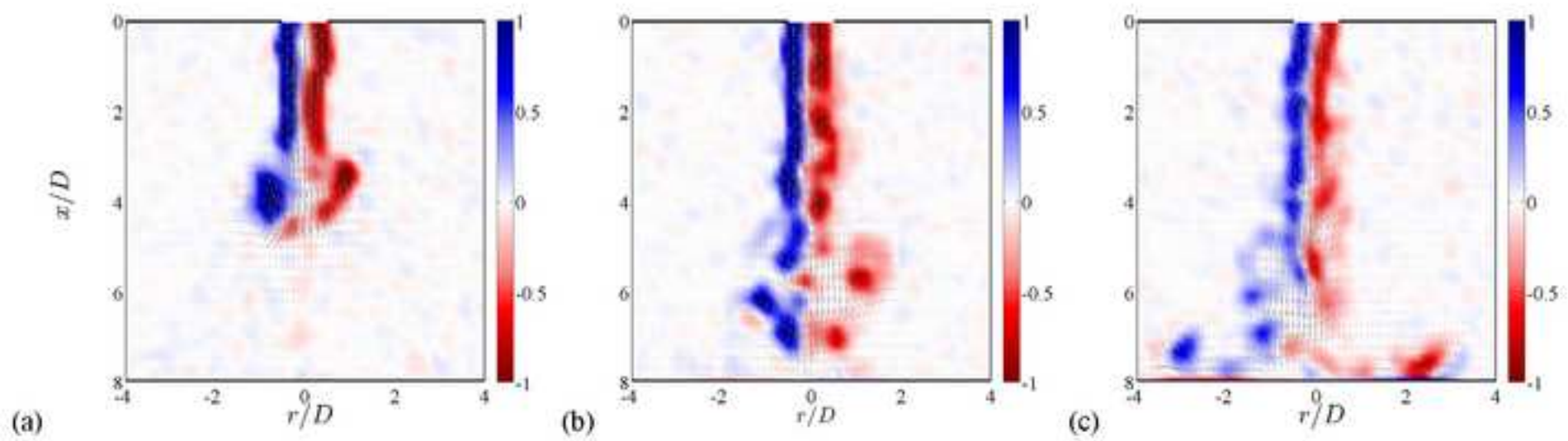
Fig. 10. Flow regime map for the axisymmetric impinging synthetic jet, as identified from PIV flow field data ($Re = 1500$, $H/D = 4, 8, 12$, and $L_0/D = 3, 4, 6, 8, 12, 16, 18$). Markers represent flow fields matching regime A (\square), regime B (\circ), and regimes C and D (\triangle). Dash-dotted lines represent the thresholds between regimes A-D (see Table 2). The horizontal dashed line is the jet formation threshold ($L_0 = L_0^{(j)} = 2D$).





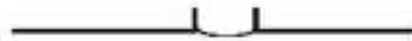








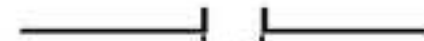
(a)



(b)

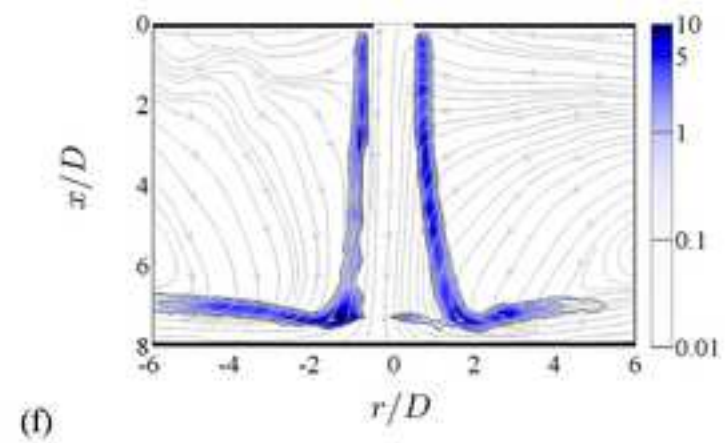
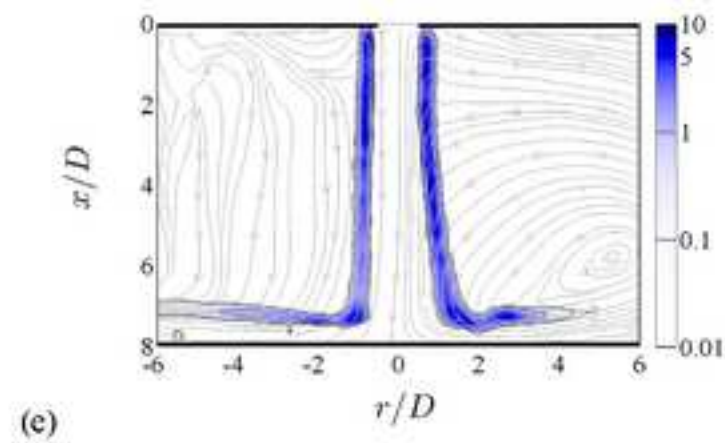
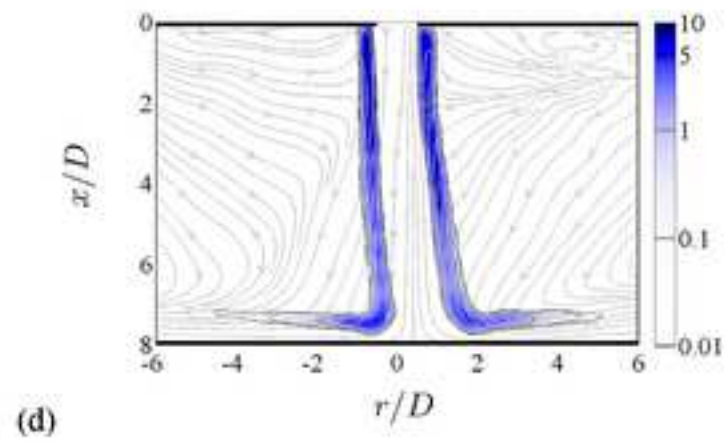
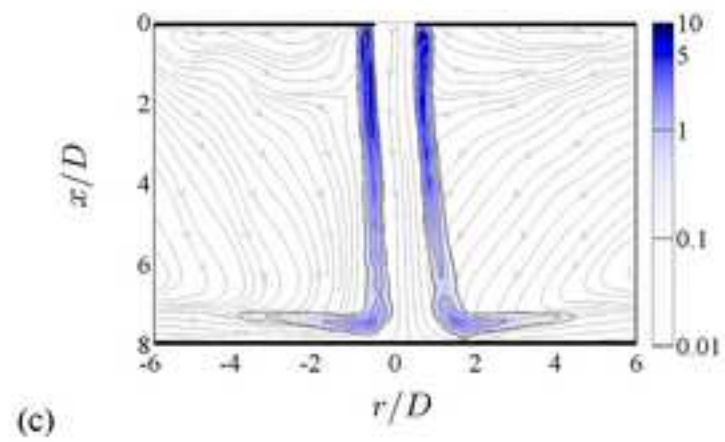
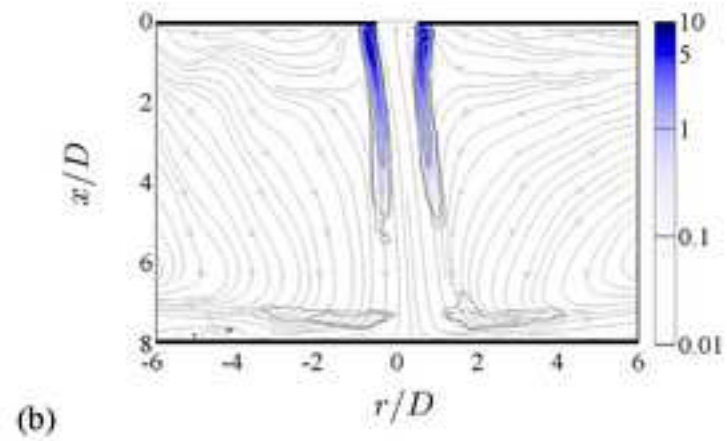
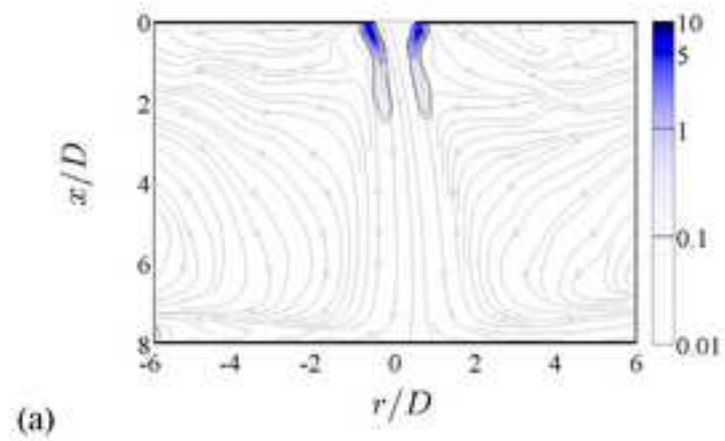


(c)

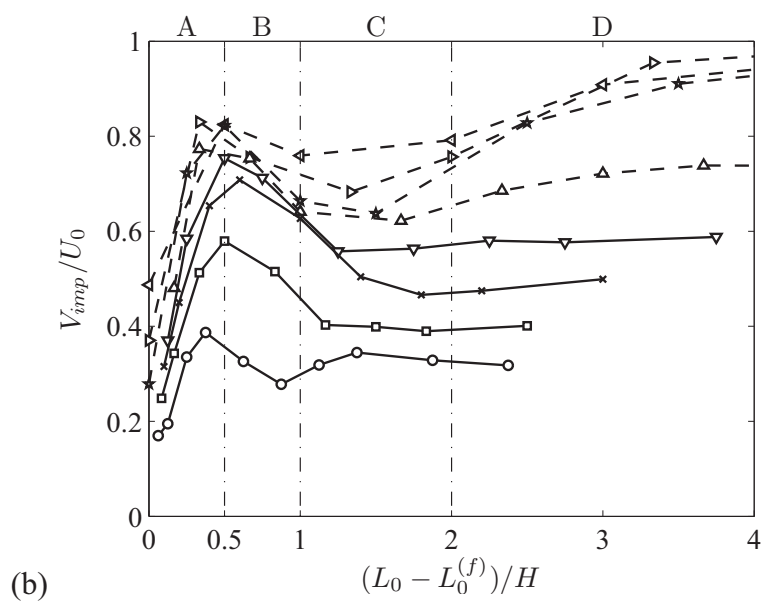
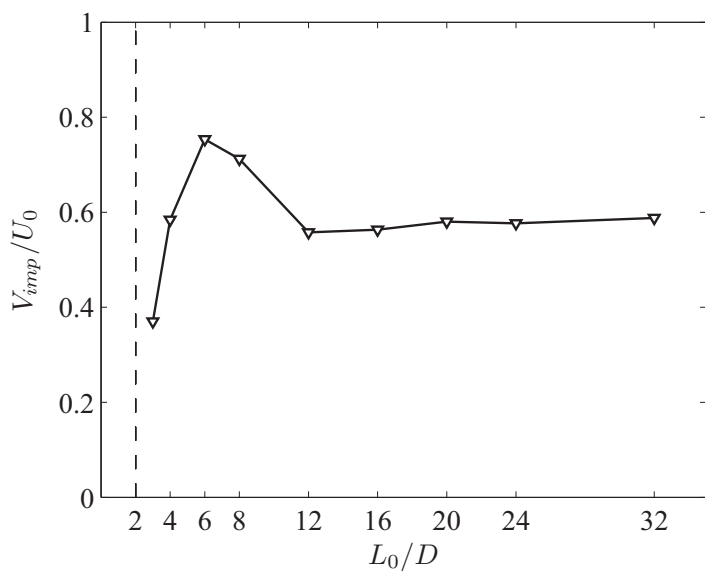


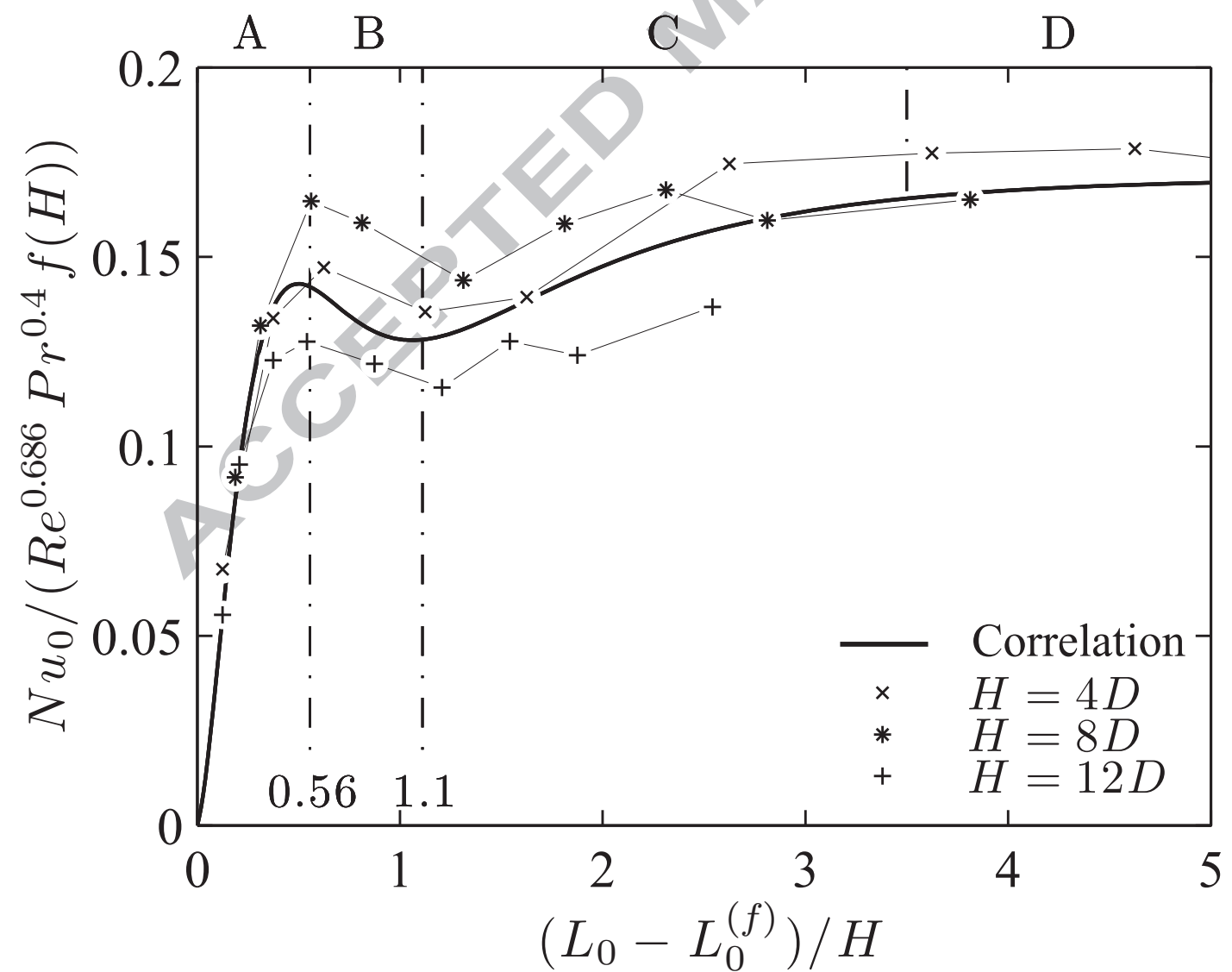
(d)

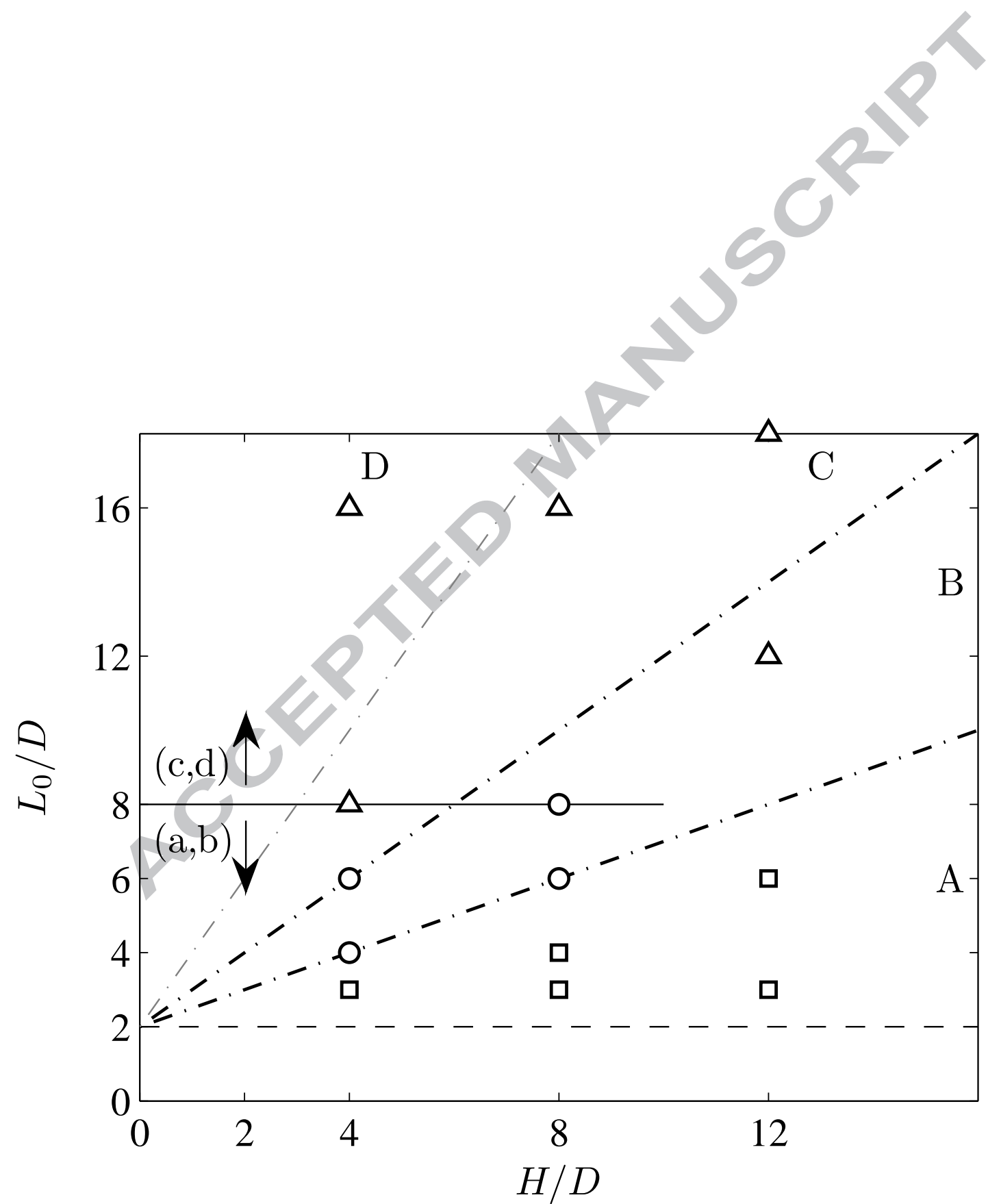
ACCEPTED



ACCEPTED MANUSCRIPT







Regime	Stroke length threshold	Corresponding figures	Description
	$L_0 \leq L_0^{(f)} (= 2D)$		No jet formed below the formation threshold stroke length **.
(a)	$L_0^{(f)}/D < L_0/D \leq 4$	Fig. 2a,b	Monotonous increase in vortex strength with stroke length up to a maximum at $L_0/D = 4$.
(b)	$4 < L_0/D \leq 8$	Fig. 3	Additional ejected fluid (beyond $L_0/D = 4$) forms a trailing jet following the vortex, resulting in a wider vortex core.
(c)	$8 < L_0/D \leq 16$	Fig. 4	Maximum ejection velocity occurs in the trailing jet, which destabilises the preceding vortex and results in increased flow mixing.
(d)	$L_0/D > 16$	Fig. 5	The flow is dominated by the trailing jet which overtakes the vortex, resulting in a highly turbulent intermittent jet flow.

** The formation threshold value $L_0^{(f)}/D = 2$ found in this study is higher than the limit proposed by e.g. Holman et al. [2], which may be attributed to minor geometric differences (e.g., a rounded orifice edge, see Eq. (4)).

Regime	Stroke length threshold	Corresponding figures	Description
	$L_0 \leq L_0^{(f)} (= 2D)$		No jet formed below the formation threshold stroke length ^{**} .
A	$0 < (L_0 - L_0^{(f)})/H \leq 0.5$	Fig. 7a,b	Diminishing impingement due to insufficient fluid momentum near the surface.
B	$0.5 < (L_0 - L_0^{(f)})/H \leq 1$	Fig. 7c,d	Optimal impingement for maximum stagnation point velocity.
C	$1 < (L_0 - L_0^{(f)})/H \leq 2$	Fig. 7e	Radial spreading/widening of the jet causing reduction in time-averaged velocity approaching the stagnation point.
D	$(L_0 - L_0^{(f)})/H > 2$	Fig. 7f	Regime dominated by the trailing jet.

^{**} The formation threshold value $L_0^{(f)}/D = 2$ found in this study is higher than the limit proposed by e.g. Holman et al. [2], which may be attributed to minor geometric differences (e.g., a rounded orifice edge, see Eq. (4)).

Highlights

- An impinging synthetic jet flow strongly dependent on the stroke length.
- High speed particle image velocimetry is combined with near-wall hot wire anemometry.
- The stroke length to nozzle diameter ratio (L_0/D) determines the free jet flow morphology.
- The stroke length to surface distance ratio (L_0/H) determines the impinging flow regime.
- Four impinging jet flow regimes found to agree well with heat transfer regimes.